INTERNATIONAL JOURNAL OF ADVANCED RESEARCH
International Peer-Reviewed Research Journal
ISSN (Online): 3106-7980 | ISSN (Print): 3106-7972
Volume 3 • Issue 2 • June 2026

LAND-COVER CHANGE AND FLOOD SUSCEPTIBILITY IN MALAKAND DIVISION, PAKISTAN, DURING THE 2010 AND 2022 FLOOD YEARS

Fazeel Ur Rehman Shahid[1], Adeel Ur Rehman Shahid[*2], Sidra Allah Wasaya[3], Kainat Bibi[4]

[1,4]*Institute of Agro- Industry and environment, Faculty of Agriculture and Environmental Sciences, The Islamia University, Bahawalpur, Pakistan*
[*2]*School of Earth Sciences and Engineering, Hohai University, Nanjing 2100987, China*
[3]*Department of zoology Punjab university new campus Lahore Pakistan*

[*2]adeelshahid@hhu.edu.cn, [3]sidraallahwasayapu@gmail.com

DOI: https://doi.org/10.5281/zenodo.24154792

Keywords
Flash floods, Landsat, land-cover change, Swat River, Panjkora River, flood susceptibility

Article History
Received: 01 May 2026
Accepted: 15 June 2026
Published: 30 June 2026

Copyright @Author
Corresponding Author: *
Adeel Ur Rehman Shahid

Abstract

Flood mapping in northern Pakistan must distinguish water observed during an event from terrain susceptible to rapid runoff or inundation. This study compared land cover, spectral indicators and mapped flood susceptibility in Malakand Division during the flood years of 2010 and 2022. Landsat-derived vegetation, water and surface-temperature maps were examined alongside precipitation, slope, drainage density, soil and five-class susceptibility maps. Reported class inventories were reconciled before interpreting differences between years. Built-up land increased from 206 to 422 km², a gain of 216 km² or 104.9% relative to its initial mapped area. Mapped water increased by 88 km², while vegetation, cropland and ice or glacier cover declined by 560, 195 and 148 km², respectively. The five classes accounted for 9,835 km² in 2010 and 9,236 km² in 2022. This difference of 599 km² limits attribution of individual losses to conversion and precludes treating the two tabulations as a closed transition inventory. The upper endpoint of the normalised difference water index was 0.70 in both years, despite the larger mapped water area in 2022. The two observations therefore illustrate how an index maximum and the extent of a classified surface can convey different information. Susceptibility maps showed recurring contrasts between the northern and southern sectors, but neither supplied a measured event footprint or water depth. The comparison identifies where independent flood observations would add the most information and establishes which changes can be quantified from the available maps. A common spatial mask, dated flood-stage observations and independent reference samples are required to estimate inundated area or assess transfer between events.

.

1. INTRODUCTION

Flood maps inform decisions at very different scales. A regional screening map can indicate where terrain favours rapid runoff, whereas an emergency response team needs to know which roads and settlements are under water at a particular time. Studies across Australia, Namibia and European river basins illustrate the variety of

spatial units used to describe flood hazard (Giurea et al., 2024; Kelly et al., 2023; Mshelia et al., 2024). The choice changes the meaning of a mapped hotspot. Risk also depends on who and what occupies the exposed area, and on how individual hazards interact (Cremen et al., 2022; Ming et al., 2022; Poussard et al., 2021; Quesada-Román & Campos-Durán, 2023).

Across catchments, the same rainfall total can produce different patterns of flooding. Basin geometry, drainage connectivity and surface condition govern the routing and storage of water. Studies combining catchment hydrology with multicriteria mapping evaluate these controls explicitly (Al Kuisi et al., 2024; Toosi et al., 2019), while research on land management and soil response explains why vegetation loss may alter runoff without establishing how much discharge occurred during a particular storm (Calil et al., 2015; Giertz et al., 2005). Translating such evidence into planning decisions requires clarity about the objective of a map and the consequences of a classification error (Billa et al., 2006; Tsakiris, 2007).

In South Asia, flood assessment spans Himalayan headwaters, agricultural plains and densely settled deltas. Work in the Teesta, Vaitarna, Ulhas and Bansloi basins has related topography and drainage to spatial differences in susceptibility (Das, 2018; Das, 2019; Hossain & Mumu, 2024; Paul et al., 2019). Bangladesh studies also show why a physically susceptible location and a socially vulnerable community require different measurements (Hoque et al., 2019; Hossain & Paul, 2018). Regional reviews identify this distinction as important for Pakistan, where event conditions and management capacity vary markedly among basins (Khan et al., 2021; Shah et al., 2020).

In Khyber Pakhtunkhwa, household studies capture dimensions of flood preparedness that cannot be inferred from optical imagery (Shah et al., 2017; Ullah et al., 2021). Provincial vulnerability and risk assessments similarly depend on information about exposure as well as environmental controls (Ibrahim et al., 2024; Ibrahim et al., 2025). Within Malakand Division, the Swat and Panjkora river systems offer particularly relevant examples: sub-watershed ranking identifies potential source areas for rapid runoff, while frequency-ratio mapping and urban assessments address different aspects of susceptibility in valley settlements (Nasir et al., 2020; Ullah & Zhang, 2020; Waseem et al., 2023). The physical area supplying runoff may lie well upstream of the fields or buildings that experience inundation.

Methods for identifying flood-prone land range from empirical frequency ratios and statistical indices to entropy-based scoring (Cao et al., 2016; Haghizadeh et al., 2017; Rahmati et al., 2016). Comparisons using regression, bivariate statistics and decision trees illustrate how class boundaries depend on the representation of observed events (Nandi et al., 2016; Tehrany et al., 2013; Tehrany et al., 2014). National-scale applications can support broad screening, while site-scale water-depth estimation requires additional elevation and event observations (Elkhrachy, 2022; Vojtek & Vojteková, 2019). These approaches answer complementary questions. In a two-date satellite comparison, adding more layers does not by itself demonstrate that the final score corresponds to observed water.

The gap addressed here is the interpretation of two flood-year map inventories that combine dynamic satellite signals with comparatively stable terrain. The practical problem is that apparent growth in water cover can reflect permanent water, acquisition season, classification or temporary flooding. This study reconciles the land-cover totals, compares paired vegetation, water and temperature maps, and interprets susceptibility in relation to rainfall, drainage, slope and soil. Its contribution is an explicit separation of measurable changes in the inventories, spatial patterns visible on the maps and event processes that require independent observations. This distinction allows the two years to be compared without attributing every difference to flood damage.

2. Materials and Methods

2.1. Study area

The mapped domain covers Malakand Division in northwestern Khyber Pakhtunkhwa. Its

elongated northern headwaters contrast with the more compact southern sector, where valley agriculture and settlements occupy terrain connected to the Swat and Panjkora drainage systems. Chitral, Upper and Lower Dir, Swat, Shangla, Buner and the Malakand area provide the geographic context used in the source report. The area totals presented below refer to individual map inventories. The administrative outline alone does not establish how many pixels were classified in either year.

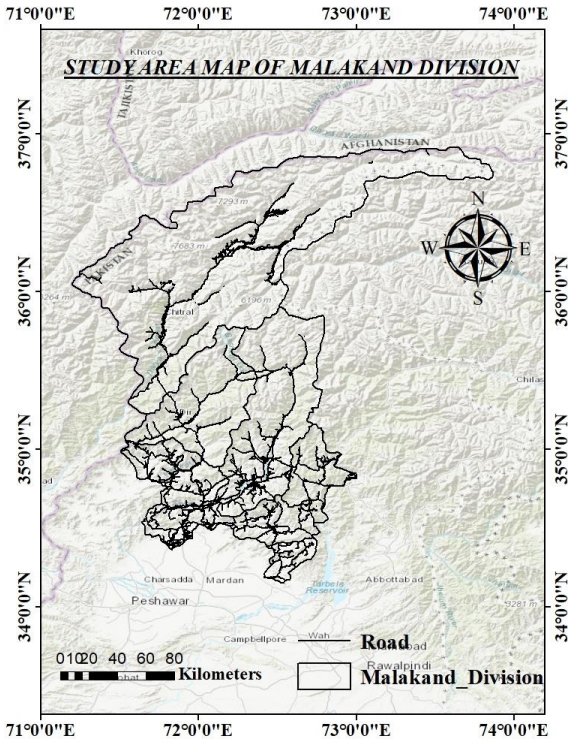


Figure 1. Location and mapped boundary of Malakand Division. The same outline appears in the paired thematic maps.

2.2. Dataset description

Table 1. Inputs, observation periods and analytical roles.

Dataset	Period or scale	Use and provenance
Landsat 5 TM and Landsat 8 OLI/TIRS	2010 and 2022; reflective bands at 30 m	Land cover, NDVI, NDWI and thermal imagery. Source report identifies Google Earth Engine access.
Precipitation grids	Two dated map products	NASA Giovanni is identified as the access portal. Product code, units and accumulation interval are unspecified.
Elevation data	30 m nominal DEM	Report names SRTM/ASTER. The source used for each terrain product is unresolved.
Drainage and soil themes	One map per variable	Spatial interpretation of drainage

		organisation and soil zones. Source edition and units of the drainage values are unspecified.
Sentinel-1 radar and field observations	Ancillary sources described in workflow	No scene identifiers, observation dates or point-level results accompany the figures.
Class inventories and final map plates	2010 and 2022	Five reported land-cover areas per year and two ordinal susceptibility maps.

The Landsat archive contains different processing levels, and native thermal support differs from the optical grid (U.S. Geological Survey, 2021). A nominal 30 m output grid alone does not establish comparable thermal resolution or atmospheric correction.

2.3. Data preprocessing and map comparison

The source workflow describes seasonal optical mosaics. For the present comparison, maps were paired by variable, year and boundary shape. Each panel was read against its own legend. Numeric results were transcribed from tabulated class inventories or legible map endpoints. Scene lists, cloud masks, solar geometry, composite dates and raster grids were unavailable. Consequently, a pair of panels labelled by year was treated as a comparison of mapped states. The dates could not be aligned to an event hydrograph.

The distinction between a baseline, an observation at flood peak and a post-event composite is especially important in steep terrain. A water signal can disappear between satellite observations, while a seasonal mosaic can combine dates with different water levels. Similar issues arise in flood mapping elsewhere in Pakistan (Haq et al., 2012). A validation inventory would need independent observations with matching dates and a documented sampling design (Foody, 2002).

2.4. Analytical methods

2.4.1. Land-cover area accounting

The five classes were water, vegetation, ice and glaciers, built-up land and cropland. Absolute and relative changes were calculated from the reported areas. For class k, A denotes area in square kilometres and the year is indicated by a subscript. Relative change uses the 2010 area of the same class.

$$\Delta A_k = A_{k,2022} - A_{k,2010},$$
$$R_k = 100\ (\Delta A_k)/A_(k, 2010) \quad (1)$$

Annual totals were compared before interpreting class changes. A complete transition matrix on a common mask must conserve total area; individual class differences alone do not determine the source or destination of a transition. Accuracy-adjusted area estimates would additionally require reference samples (Olofsson et al., 2014).

2.4.2. Spectral and thermal indicators

NDVI describes the contrast between near-infrared and red reflectance (Tucker, 1979). The green and near-infrared formulation of NDWI accentuates open water under suitable illumination (McFeeters, 1996). Both indices are dimensionless. In Equations 2 and 3, ρ denotes reflectance in the indicated band.

$$\mathrm{NDVI} = \frac{\rho_{\mathrm{NIR}} - \rho_{\mathrm{red}}}{\rho_{\mathrm{NIR}} + \rho_{\mathrm{red}}} \quad (2)$$

$$\mathrm{NDWI} = \frac{\rho_{\mathrm{green}} - \rho_{\mathrm{NIR}}}{\rho_{\mathrm{green}} + \rho_{\mathrm{NIR}}} \quad (3)$$

The source workflow proposes a positive NDWI threshold for candidate water. A modified index using shortwave infrared offers an alternative where built land confounds open-water mapping (Xu, 2006). Neither rule establishes temporary inundation without a pre-event land/water reference. Thermal panels were compared using the map endpoints and within-year spatial ordering. The reported workflow mentions emissivity correction, but supplies no calibration parameters, acquisition times or independent surface-temperature measurements.

2.4.3. Terrain, drainage and susceptibility

Slope is a local derivative of the elevation surface and depends on the grid and derivative operator (Horn, 1981). Drainage density is conventionally defined as the length of the stream network divided by catchment area (Horton, 1945). Equation 4 gives the definition for a set of mapped reaches with lengths L_i and a contributing area A. The original drainage map omits its unit, so its legend was interpreted ordinally.

$$D_d = \frac{\sum_i L_i}{A} \qquad (4)$$

The workflow combines terrain, hydrography, land cover and spectral indicators. A weighted overlay ordinarily requires criterion scores, weights and class cutoffs (Malczewski, 2000). The original project does not give these parameters. The two resulting five-class maps were therefore examined as ordinal products. Although random forest and support vector machines are listed in the workflow, training data, fitted models and predictions are unavailable. Published flood-classification applications illustrate the additional evidence required to evaluate a trained model (Wang et al., 2015).

2.4.4. Evidence for validation and transfer

Matched event footprints, independent class labels and model outputs were sought in the report. References to GPS, UAV observations, flood marks and hydraulic comparisons were distinguished from records of specific observations. No confusion matrix, sampled coordinates, depth residuals or held-out event predictions accompany the maps. Assessment was consequently restricted to internal consistency and visual comparison. Model transfer accuracy, discharge and event-specific flood depths were outside the evidence available for this analysis.

3. Results

3.1. Land-cover change and the classified footprint

Built-up land more than doubled in the reported inventory, from 206 to 422 km². Water increased from 314 to 402 km². Vegetation showed the largest absolute decrease, losing 560 km², followed by cropland at 195 km² and ice or glacier cover at 148 km². Relative to its smaller initial extent, the ice/glacier class declined more sharply than vegetation. Table 2 separates relative change within each class from change in the sum of all listed classes.

Table 2. Reported land-cover areas and changes calculated from the two inventories.

Class	2010 (km²)	2022 (km²)	Change (km²)	Change (%)
Water	314	402	+88	+28.0
Vegetation	3,780	3,220	-560	-14.8
Ice and glaciers	825	677	-148	-17.9
Built-up	206	422	+216	+104.9
Cropland	4,710	4,515	-195	-4.1
Listed classes	9,835	9,236	-599	-6.1

The two positive changes totalled 304 km², whereas the three decreases totalled 903 km². Their difference matches the 599 km² shortfall between inventories. Even if all additional built-up land had previously been vegetated, that hypothetical transition alone could not account for the 560 km² reduction in vegetation. The data do not determine which transitions occurred.

3.2. Land cover in 2010

Cropland was the largest of the five reported classes, followed by vegetation. Together they accounted for 8,490 km², or 86.3% of the listed area. The 2010 plate shows a fine interspersion of mapped classes across the southern body and elongated bands in the north. Built-up land represented only 2.1% of the area inventory despite the prominence of its strongly contrasting legend colour. The visual salience of a class

should therefore be read alongside its reported area.

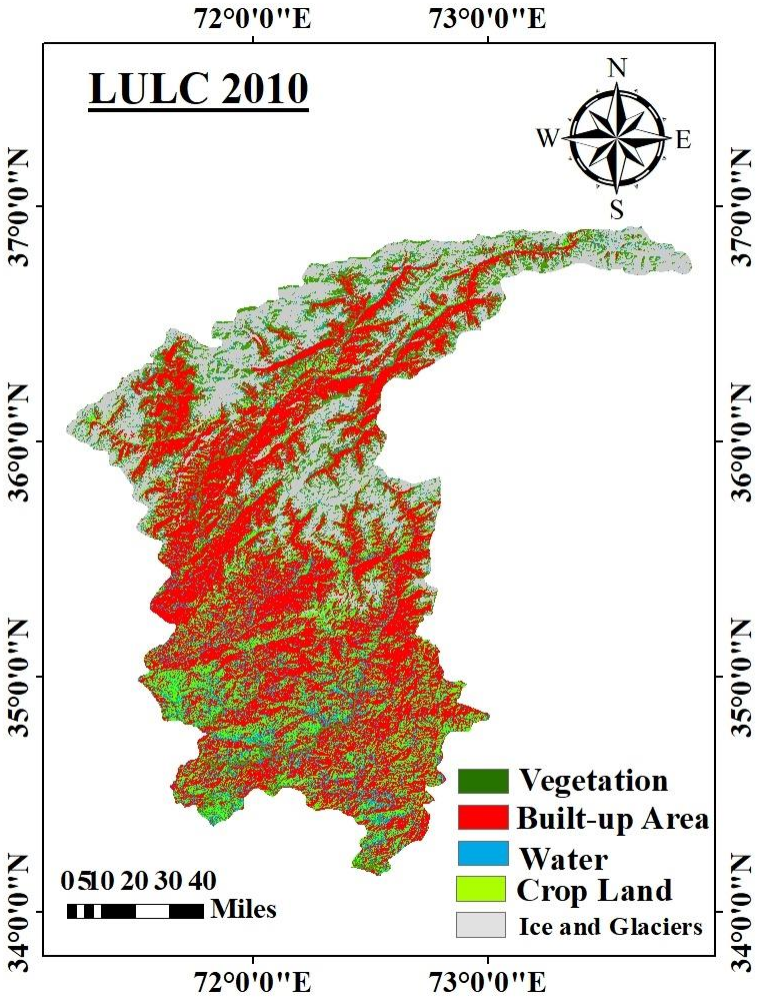


Figure 2. Five-class Landsat-era land-cover map for 2010.

3.3. Land cover in 2022

Cropland and vegetation remained the two largest listed classes, totalling 7,735 km². Their combined share of the 2022 inventory was 83.7%. Built-up land reached 4.6% when calculated against the sum of listed classes for that year. This differs from the source narrative's 4.3%, which uses an apparently different denominator. The class ranking is robust to that distinction, but changes in class shares cannot substitute for an overlay on a common mask.

INTERNATIONAL JOURNAL OF ADVANCED RESEARCH
International Peer-Reviewed Research Journal
ISSN (Online): 3106-7980 | ISSN (Print): 3106-7972
Volume 3 • Issue 2 • June 2026

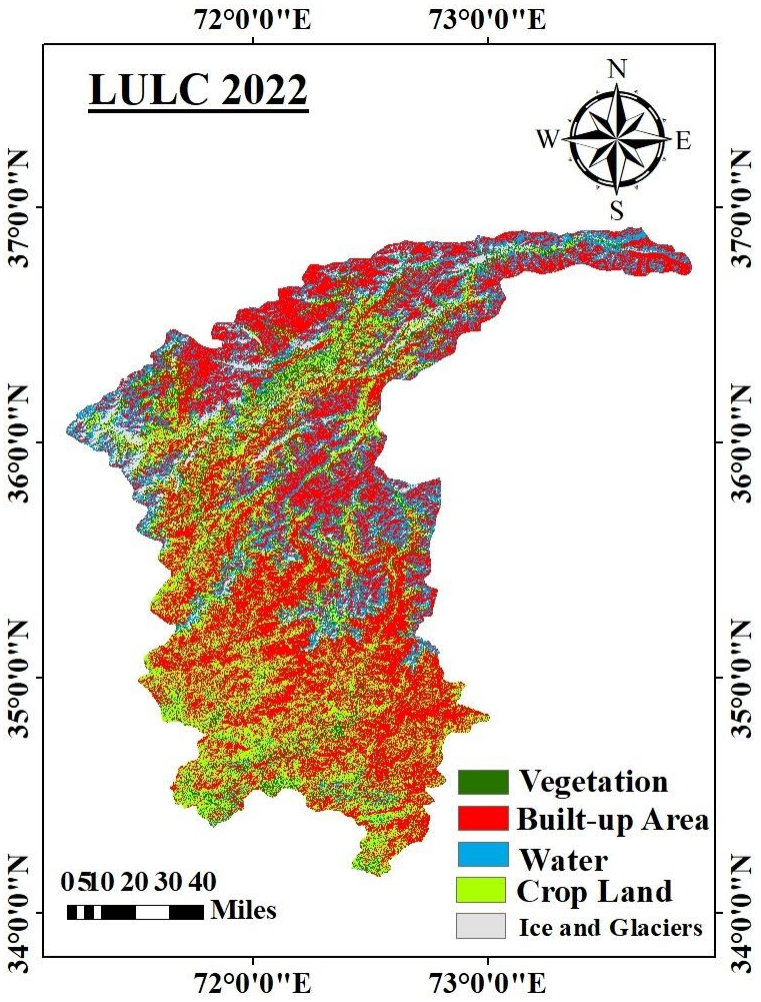


Figure 3. Land cover in 2022. Colour assignments differ from the 2010 plate and must be read using the year-specific legend.

3.4. Spatial pattern of mapped transitions

The transition plate distinguishes persistence from changes between named classes. Green and yellow categories dominate much of the display, with elongated bands in the northern sector and more closely interspersed patches farther south. Twenty-five possible origin–destination combinations exist for five classes. The legend identifies combinations, but the report gives no accompanying cell counts. The map therefore shows where transitions were assigned without providing measured gross losses, gross gains or the area converted specifically from cropland to built land.

INTERNATIONAL JOURNAL OF ADVANCED RESEARCH
International Peer-Reviewed Research Journal
ISSN (Online): 3106-7980 | ISSN (Print): 3106-7972
Volume 3 • Issue 2 • June 2026

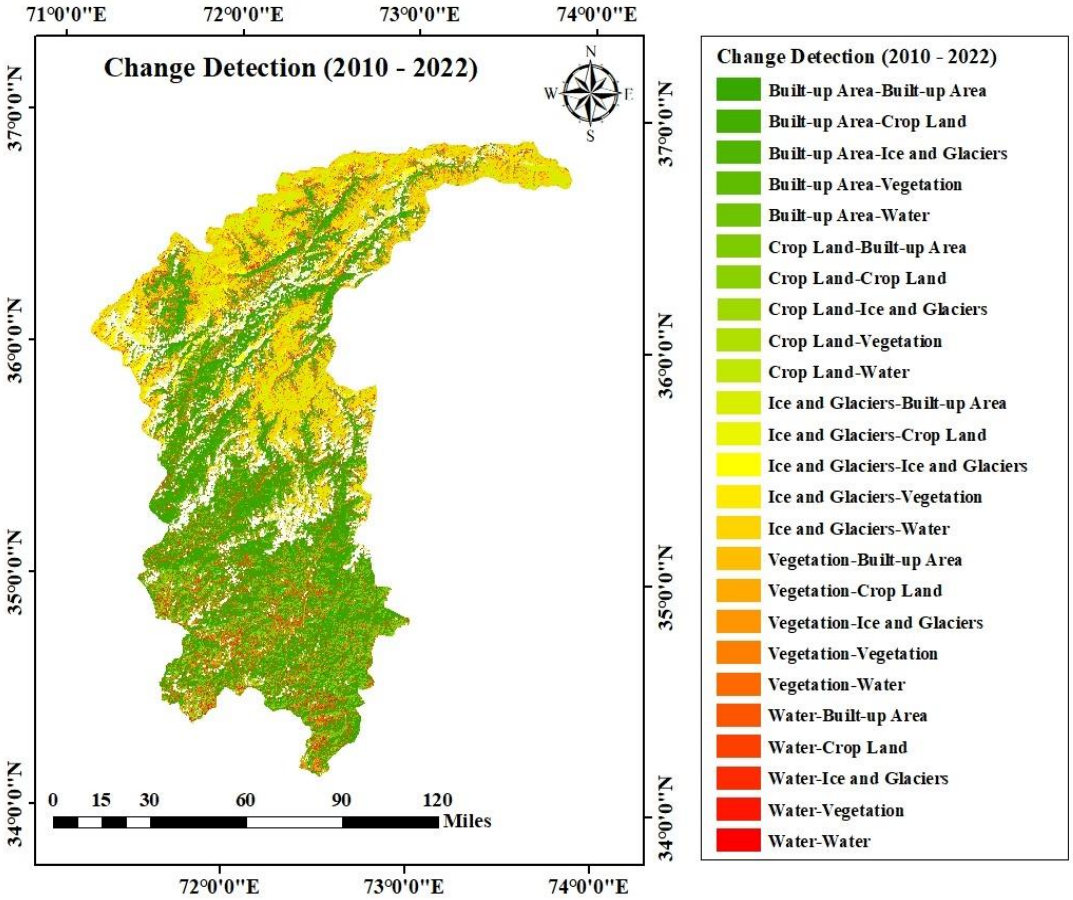


Figure 4. Class-to-class transition map between the two observations. Each legend entry specifies an origin and destination.

3.5. Vegetation-index distribution in 2010

The NDVI legend spans −0.57 to 0.72. Higher values are visible in parts of the southern sector, while the elongated northern sector contains extensive lower-value areas. The spatial gradient follows the colour ramp of this particular plate: green is at the low end and warmer colours lie toward the high end. The domain-wide extrema include many surface types. They do not describe crop-specific greenness or vegetation condition on the flood date.

INTERNATIONAL JOURNAL OF ADVANCED RESEARCH
International Peer-Reviewed Research Journal
ISSN (Online): 3106-7980 | ISSN (Print): 3106-7972
Volume 3 • Issue 2 • June 2026

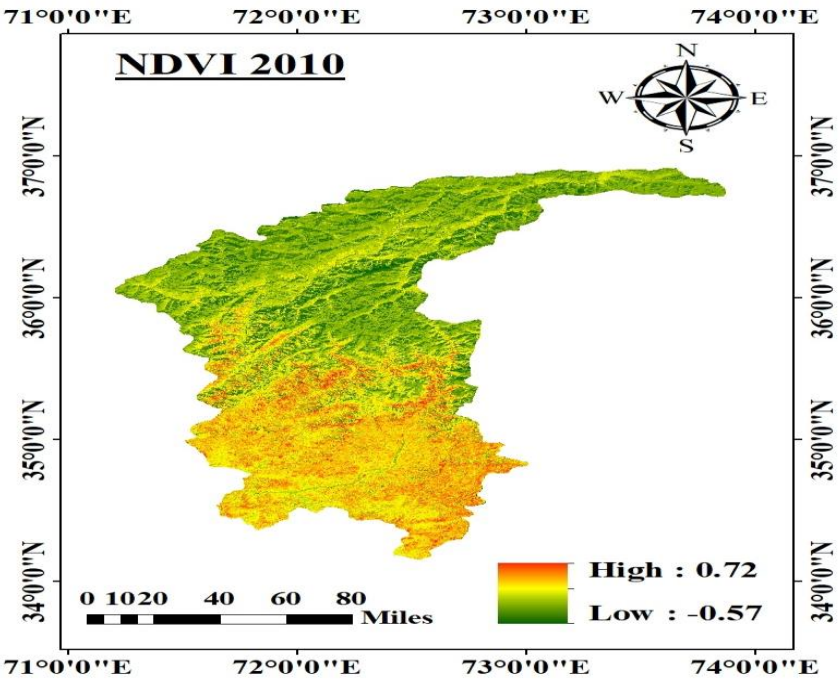


Figure 5. Normalised difference vegetation index for 2010.

3.6. Vegetation-index distribution in 2022

The 2022 NDVI maximum was 0.77 and its minimum was −0.70. The full displayed range therefore widened from 1.29 to 1.47. Both a higher maximum and a lower minimum contributed to that increase. A broader range is compatible with greater contrast among mapped surfaces, but does not establish an increase or decrease in mean vegetation condition. The southern and northern sectors retain contrasting colour distributions. The two maps contain no dated sequence from which to measure recovery in days or months.

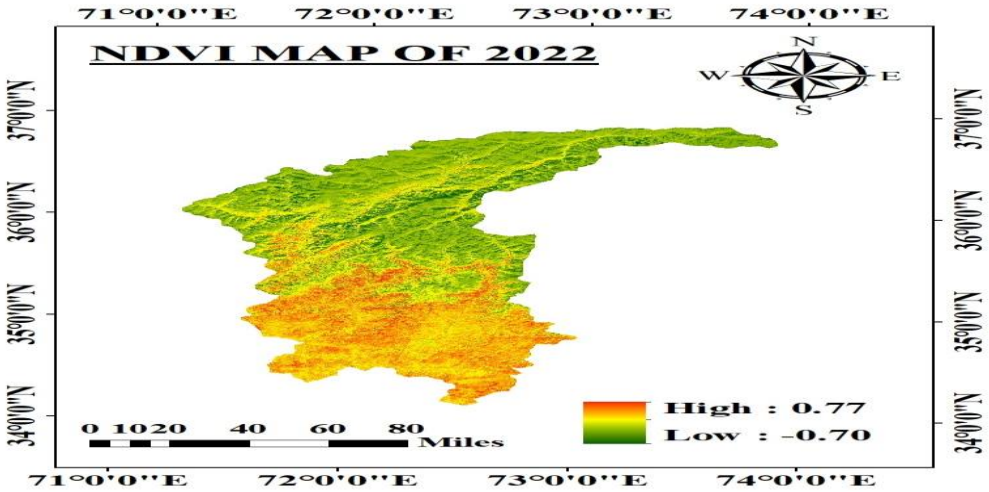


Figure 6. Normalised difference vegetation index for 2022; compare with Figure 5 using numerical legend values.

3.7. Optical water signal in 2010

The 2010 NDWI ranges from −0.72 to 0.70. The southern sector contains many green-to-blue pixels, while portions of the northern arm show lighter green and yellow values. Strong positive index values are consistent with open water, but the extremes do not show whether a location was dry before the flood. The reported 314 km² water inventory includes water as a land-cover category. It is consequently a different measure from the area temporarily inundated in 2010.

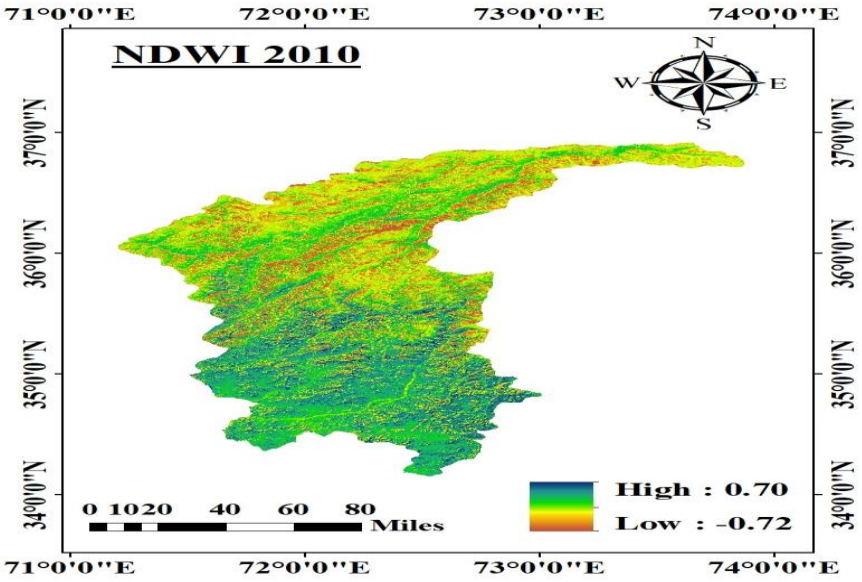


Figure 7. Normalised difference water index for 2010.

3.8. Optical water signal in 2022

The positive endpoint remained 0.70, while the negative endpoint shifted from −0.72 to −0.84. Thus the mapped water class grew by 28.0% relative to its 2010 area even though the maximum NDWI was unchanged. One measure counts classified area and the other identifies an extreme reflectance contrast. Neither measures water depth. Demonstrating newly flooded land would require pixel-level changes from dry to wet within an event window and a mask for permanent or seasonal water.

INTERNATIONAL JOURNAL OF ADVANCED RESEARCH
International Peer-Reviewed Research Journal
ISSN (Online): 3106-7980 | ISSN (Print): 3106-7972
Volume 3 • Issue 2 • June 2026

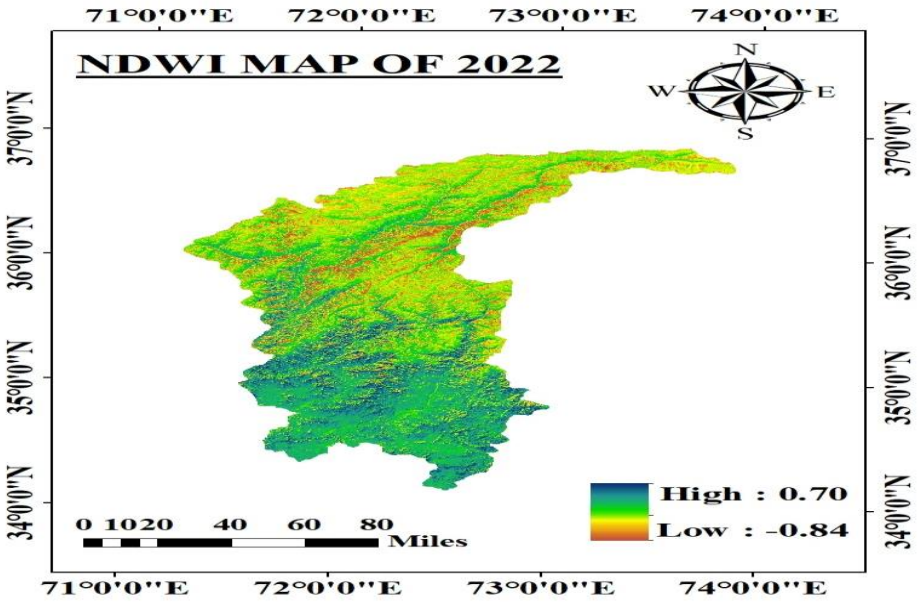


Figure 8. Normalised difference water index for 2022.

3.9. Thermal organisation in 2010

The thermal map ranges from −6.87 to 46.37 °C. Its four legend intervals use red for the coldest class and green for the warmest. Cold surfaces form extensive patches across the northern arm, whereas warmer classes occupy a greater visible portion of the south. This is a regional contrast across a mountainous domain. A cold pixel near a drainage line cannot be identified as floodwater solely from its temperature because elevation, snow and terrain shadow can produce similar contrasts.

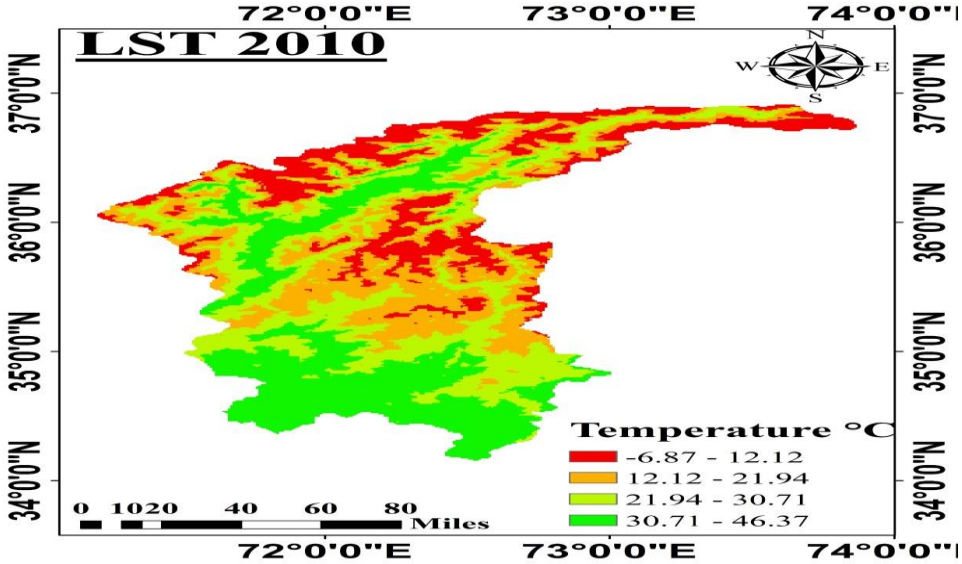


Figure 9. Land surface temperature in 2010. Map classes are defined in degrees Celsius.

3.10. Thermal organisation in 2022

The 2022 legend spans −5.95 to 48.91 °C. The upper endpoint was 2.54 °C higher than in 2010, and the lower endpoint was 0.92 °C higher. The classes again distinguish colder northern surfaces from widespread warmer southern surfaces. These differences compare the endpoints of two mapped products rather than matched observations of the same location. With no acquisition dates or daily series, they cannot establish nighttime warming, event-induced cooling or the duration of waterlogging.

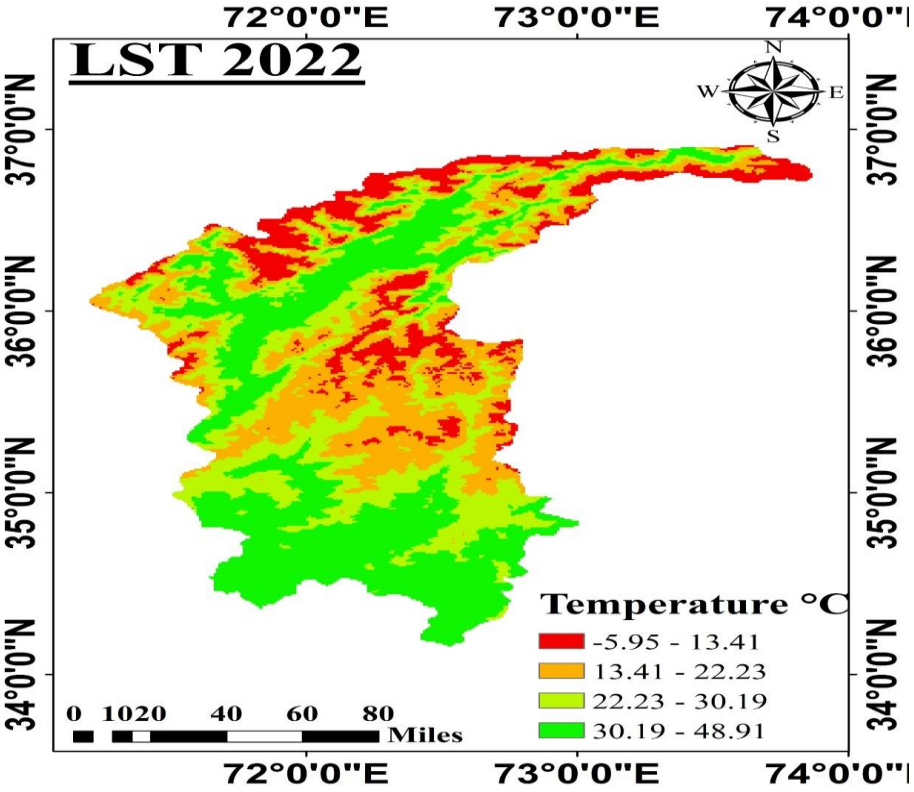


Figure 10. Land surface temperature in 2022. Class breaks differ from those used in Figure 9.

3.11. Rainfall pattern in 2010

The northern extension of the 2010 rainfall plate is predominantly pale, with stronger values in parts of the central and southern map. A central band and a southern concentration are visible against the lower northern background. The raster represents a spatial gradient across the domain. The project identifies Giovanni as the source portal but does not identify the product variable, its accumulation interval or its units on the map. The pattern therefore cannot be converted into storm intensity or a peak hourly rainfall rate.

INTERNATIONAL JOURNAL OF ADVANCED RESEARCH
International Peer-Reviewed Research Journal
ISSN (Online): 3106-7980 | ISSN (Print): 3106-7972
Volume 3 • Issue 2 • June 2026

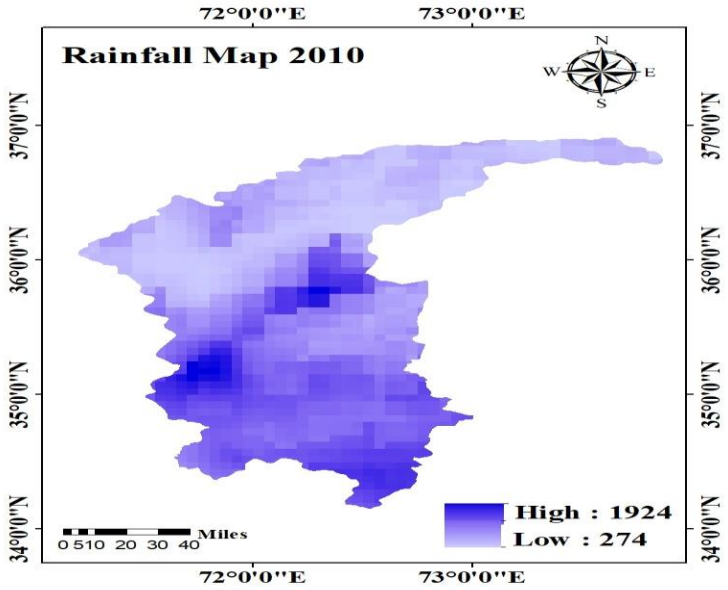


Figure 11. Rainfall product labelled 2010. Darker shading denotes larger mapped values.

3.12. Rainfall pattern in 2022

The 2022 plate retains a broad north–south gradient, but the relative prominence of darker patches changes within the southern and western parts of the mapped area. A difference between the two colour patterns does not show that a storm lasted longer at any one location. The narrative reports both district/month values and substantially different event totals, without linking those quantities to the map legend. Interpretation here is restricted to within-map spatial ordering.

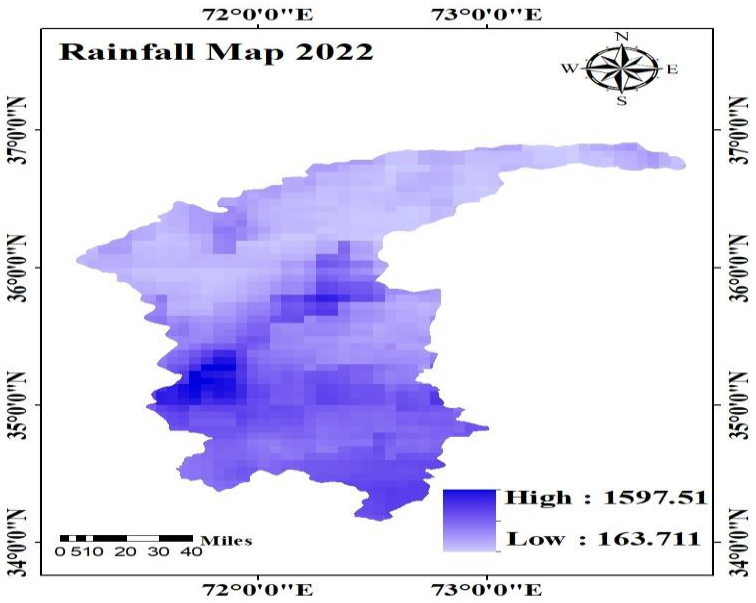


Figure 12. Rainfall product labelled 2022. Panel-specific scales and undocumented aggregation limit comparisons of event totals.

3.13. Drainage organisation

The drainage-density surface shows elongated bands crossing the northern and central sectors and further bands in the southern lobe. These patterns identify variation in the mapped network concentration. The source text expresses density in kilometres per square kilometre, whereas the plate has a different numerical range and does not print a unit. Its values are therefore not assigned physical units here. A high mapped value indicates a relative network concentration and cannot determine how rapidly a particular storm produced a flood peak.

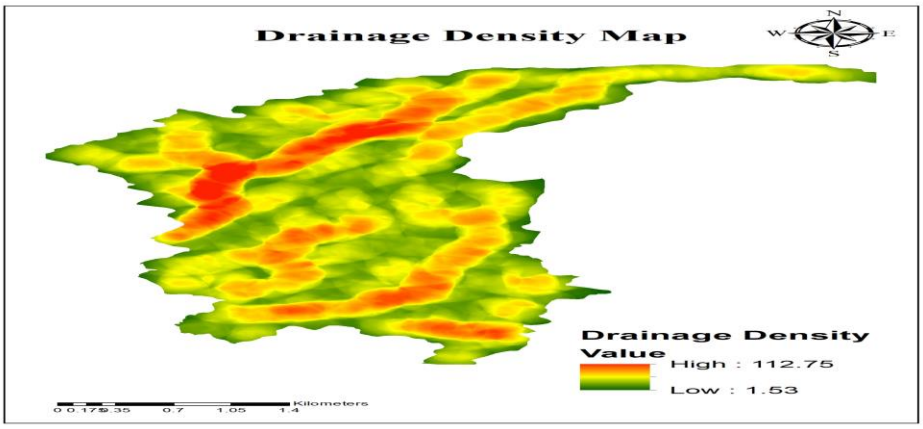


Figure 13. Drainage-density surface. The mapped numerical values lack a documented unit conversion.

3.14. Slope distribution

The slope inventory reports 2,368 km² below 15°, 4,052 km² from 15° to 30°, and 3,412 km² above 30°. Together these bands sum to 9,832 km². The middle band accounts for 41.2% of this inventory, making it the largest category. Combining the middle and steep bands places approximately 75.9% of the reported area at or above 15° under the stated class convention. These figures describe terrain distribution. They do not identify the proportion of measured discharge or landslides supplied by each band.

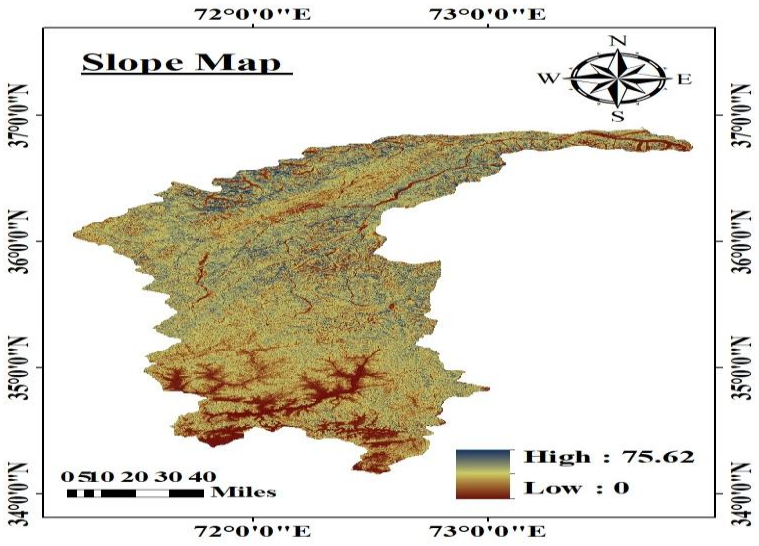


Figure 14. Slope derived from the elevation surface. Area figures in the text come from the reported slope inventory.

3.15. Soil representation

The soil layer is considerably coarser in appearance than the spectral and terrain maps. Large contiguous polygons occupy different parts of the region, in contrast to the fine within-valley variation on the Landsat products. Intersecting a broad soil polygon with a high-resolution optical image would assign a common soil label to many spectrally different pixels. The map supports regional context for drainage conditions, but cannot determine field-scale infiltration rates or the number of days that water remained on a specific plot.

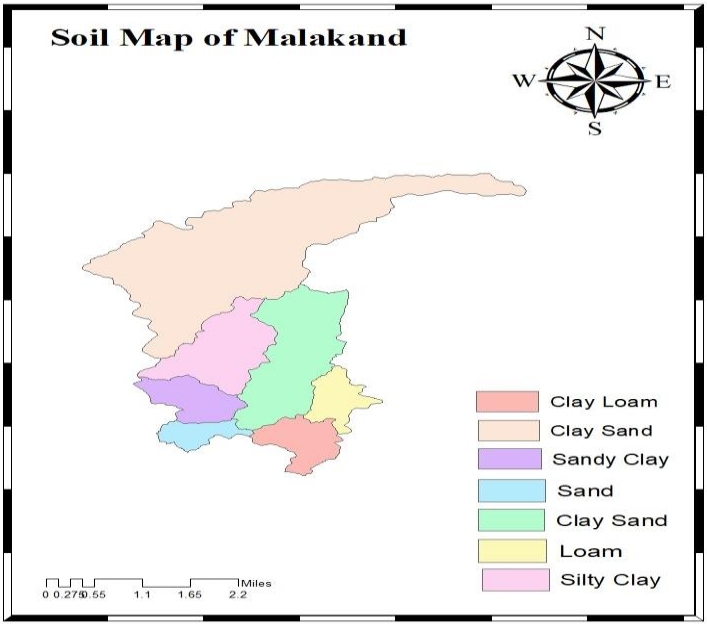


Figure 15. Soil classes represented by regional polygons.

3.16. Susceptibility during the 2010 flood year

The final map displays five ordinal colours. Higher classes are prominent across parts of the northern arm, while green lower classes occupy much of the southern map. The pattern is discontinuous, with local higher and lower patches inside both sectors. The highest legend entry is abbreviated in the original plate. The spatial pattern represents the project's composite classification; a high-ranked upland cell may identify terrain associated with rapid runoff even where the cell was never submerged.

INTERNATIONAL JOURNAL OF ADVANCED RESEARCH
International Peer-Reviewed Research Journal
ISSN (Online): 3106-7980 | ISSN (Print): 3106-7972
Volume 3 • Issue 2 • June 2026

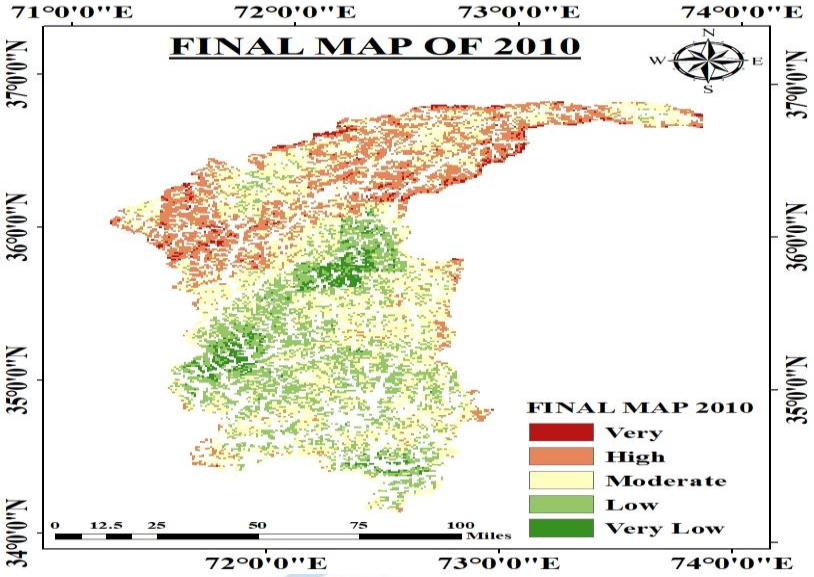


Figure 16. Composite flood susceptibility for 2010. Red denotes the upper end of the original ordinal scale.

International Journal of Advanced Research

3

.17. Susceptibility during the 2022 flood year

The 2022 product retains the broad ordering visible in 2010, with higher ranks recurring in the northern sector and lower ranks widespread farther south. Similarity is plausible because slope, drainage and soil were shared across the analysis. It does not independently validate either map or demonstrate that the same places flooded twice. The two products lack class-area totals and a common pixel transition matrix, so the magnitude of movement between susceptibility classes cannot be quantified.

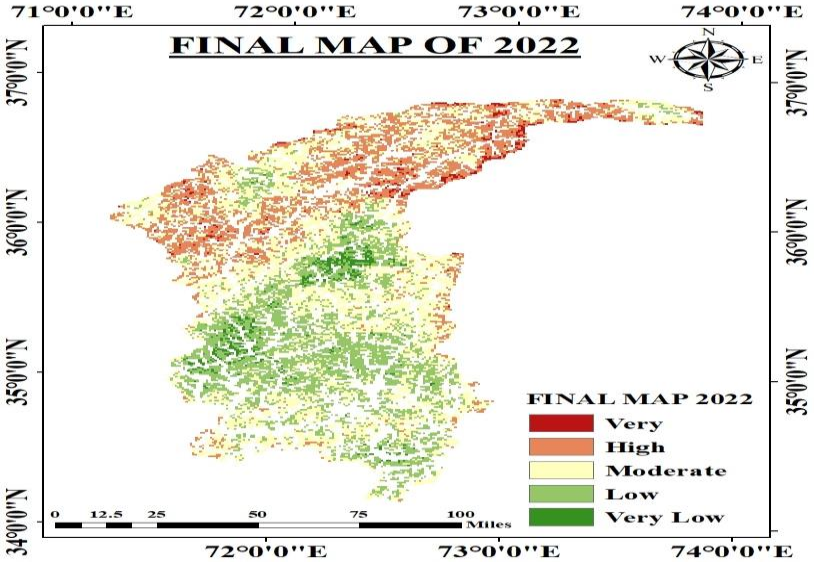


Figure 17. Composite flood susceptibility for 2022. Compare the relative geography with Figure 16.

4. Discussion

4.1. What changed between the two inventories?

The clearest result is growth in the area assigned to built land. Its absolute gain was smaller than the vegetation loss, but its proportional gain exceeded that of every other class. The observed increase is relevant to valley-floor development because changes in impervious cover can alter runoff pathways. Establishing that urban expansion intensified either flood, however, would require the location of new development relative to contributing catchments, its timing and a rainfall–runoff comparison. An increase in a regional built-up class does not supply that causal evidence.

The discrepancy between inventories changes the interpretation of the agricultural and vegetation results. Across a fixed domain with exhaustive classes, losses from one class must reappear as gains in another. Here the reported losses exceed gains by 599 km². The deficit could arise from differences in valid coverage, an omitted class or a tabulation error; the available maps do not distinguish those explanations. The area of crop-to-built conversion is therefore unresolved even though the directions of the two reported class changes are clear.

The spectral results give a separate reason for caution. A constant upper NDWI endpoint coexists with a larger classified water area. A widened NDVI range coexists with a smaller vegetation inventory. These are compatible observations because the extremes can be determined by a small number of pixels while class areas depend on the spatial distribution of all valid pixels. Neither comparison measures temporary flooding on cropland. The thermal and rainfall surfaces provide additional context, but their dates and temporal support are insufficient for estimating flood duration.

4.2. Relation to published work

Hydraulic modelling of the Swat River has combined terrain and two-dimensional flow simulation to estimate flood hazard along the channel (Farooq et al., 2019). That work clarifies what is missing from an ordinal regional overlay: a water-surface calculation linked to discharge and floodplain geometry. The Malakand maps cover a much wider range of terrain and can identify candidate subcatchments for closer examination. Comparing an upland susceptibility score directly with modelled river depth would conflate runoff generation with downstream inundation.

Hydrodynamic work along the China–Pakistan Economic Corridor similarly evaluates flood behaviour through physically connected flow pathways (Sun et al., 2023). The connected pathway matters in Malakand, where a high-scoring headwater and a lower-scoring settled valley can participate in the same event. A satellite map of standing water may predominantly record the valley response, while a terrain-based susceptibility layer emphasises the headwater contribution. That spatial separation provides a reason to maintain both products in a monitoring workflow.

Empirical comparisons of flash-flood susceptibility models show that rankings depend on how past events and conditioning factors are represented (Khosravi et al., 2016). More recent work on multi-hazard learning and alternative forecasting architectures illustrates how performance must be evaluated for a defined target and test sample (Shafizadeh-Moghadam et al., 2018; Ullah et al., 2022). For the present case, applying the same colour scheme to two final maps offers no evidence of transfer performance. Independent 2022 labels withheld from calibration on 2010 would permit a direct test of transfer across events.

4.3. Priorities for event reconstruction

The first priority is a common spatial mask and a complete area transition matrix. A reanalysis could retain cloud, snow, shadow and missing observations as explicit quality categories and calculate each comparison over the intersection of valid observations. Within that mask, newly wet pixels would require a dry baseline, a dated event observation and screening for persistent or seasonal water. The resulting area should be accompanied by independent reference labels and uncertainty intervals.

Rainfall should be identified by product name, version, physical unit and accumulation window. Daily or subdaily precipitation and hydrographs would allow temporal ordering of rainfall and downstream response. Georeferenced flood marks, independent radar acquisitions and records of blocked or breached channels would then permit validation of the inferred footprint. These observations are especially important where buildings, narrow channels or valley shadows occupy a substantial fraction of a Landsat pixel.

5. Conclusion

The two Malakand inventories record a 216 km² increase in built-up land and an 88 km² increase in water between 2010 and 2022. Vegetation, cropland and ice or glacier cover declined in the listed classes. Because their total area falls from 9,835 to 9,236 km², the class differences cannot be interpreted as a complete account of land conversion. The unchanged upper NDWI endpoint despite the larger water inventory demonstrates why spectral extrema and mapped extent should be reported separately.

Terrain and drainage organise the broad geography of the susceptibility maps, while the optical, thermal and rainfall plates describe different aspects of the two flood years. The maps are suitable for identifying areas where screening warrants event-specific investigation. Establishing flood extent, depth, agricultural damage or predictive transfer requires matched event observations, a common valid-data mask and independent validation. Recovering the original rasters and scene metadata would materially improve the value of the existing regional analysis.

REFERENCES

Al Kuisi, M., Al Azzam, N., Hyarat, T., & Farhan, I. (2024). Flood hazard and risk assessment of flash floods for Petra catchment area using hydrological and analytical hierarchy (AHP) modeling. Water, 16, 2283. https://doi.org/10.3390/w16162283

Billa, L., Shattri, M., Rodzi Mahmud, A., & Halim Ghazali, A. (2006). Comprehensive planning and the role of SDSS in flood disaster management in Malaysia. Disaster Prev. Manag., 15, 233–240. https://doi.org/10.1108/09653560610659775

Calil, J., Beck, M. W., Gleason, M., Merrifield, M., Klausmeyer, K., & Newkirk, S. (2015). Aligning natural resource conservation and flood hazard mitigation in California. PLoS ONE10, e0132651. https://doi.org/10.1371/journal.pone.0132651

Cao, C., Xu, P., Wang, Y., Chen, J., Zheng, L., & Niu, C. (2016). Flash flood hazard susceptibility mapping using frequency ratio and statistical index methods in coalmine subsidence areas. Sustainability, 8, 948. https://doi.org/10.3390/su8090948

Cremen, G., Galasso, C., & McCloskey, J. (2022). Modelling and quantifying tomorrow's risks from natural hazards. Sci. Total Environ., 817, 152552. https://doi.org/10.1016/j.scitotenv.2021.152552

Das, S. (2018). Geographic information system and AHP-based flood hazard zonation of Vaitarna basin, Maharashtra, India. Arabian J. Geosciences, 11, 576. https://doi.org/10.1007/s12517-018-3933-4

Das, S. (2019). Geospatial mapping of flood susceptibility and hydro-geomorphic response to the floods in Ulhas basin, India. Remote Sens. Appl. Soc. Environ., 14, 60–74. https://doi.org/10.1016/j.rsase.2019.02.006

Elkhrachy, I. (2022). Flash flood water depth estimation using SAR images, digital elevation models, and machine learning algorithms. Remote Sens., 14, 440. https://doi.org/10.3390/rs14030440

Farooq, M., Shafique, M., & Khattak, M. S. (2019). Flood hazard assessment and mapping of River Swat using HEC-RAS 2D model and high-resolution 12-m TanDEM-X DEM (WorldDEM). Nat. Hazards, 97, 477–492. https://doi.org/10.1007/s11069-019-03638-9

Foody, G. M. (2002). Status of land cover classification accuracy assessment. Remote Sensing of Environment, 80(1), 185–201. https://doi.org/10.1016/S0034-4257(01)00295-4

Giertz, S., Junge, B., & Diekkrüger, B. (2005). Assessing the effects of land use change on soil physical properties and hydrological processes in the sub-humid tropical environment of West Africa. Phys. Chem. Earth, Parts A/B/C30, 485–496. https://doi.org/10.1016/j.pce.2005.07.003

Giurea, A., Comănescu, L., Dobre, R., Nedelea, A., & Mirea, I. (2024). Flood risk assessment using multi-criteria spatial analysis case study: Gilort river between Bălceşti and Bolboceşti. Water, 16, 1760. https://doi.org/10.3390/w16131760

Haghizadeh, A., Siahkamari, S., Haghiabi, A. H., & Rahmati, O. (2017). Forecasting flood-prone areas using Shannon's entropy model. J. Earth Syst. Sci., 126, 39–11. https://doi.org/10.1007/s12040-017-0819-x

Haq, M., Akhtar, M., Muhammad, S., Paras, S., & Rahmatullah, J. (2012). Techniques of remote sensing and GIS for flood monitoring and damage assessment: A case study of Sindh province, Pakistan. The Egyptian Journal of Remote Sensing and Space Sciences, 15(2), 135–141. https://doi.org/10.1016/j.ejrs.2012.07.002

Hoque, M. A.-A., Tasfia, S., Ahmed, N., & Pradhan, B. (2019). Assessing spatial flood vulnerability at Kalapara Upazila in Bangladesh using an analytic hierarchy process. Sensors, 19, 1302. https://doi.org/10.3390/s19061302

Horn, B. K. P. (1981). Hill shading and the reflectance map. Proceedings of the IEEE, 69(1), 14–47. https://doi.org/10.1109/PROC.1981.11918

Horton, R. E. (1945). Erosional development of streams and their drainage basins: Hydrophysical approach to quantitative morphology. Geological Society of America Bulletin, 56(3), 275–370. https://doi.org/10.1130/0016-7606(1945)56[275:EDOSAT]2.0.CO;2

Hossain, M. N., & Mumu, U. H. (2024). Flood susceptibility modelling of the Teesta River Basin through the AHP-MCDA process using GIS and remote sensing. Nat. Hazards, 120, 12137–12161. https://doi.org/10.1007/s11069-024-06677-z

Hossain, M. N., & Paul, S. K. (2018). Vulnerability factors and effectiveness of disaster mitigation measures in the Bangladesh coast. Earth Syst. Environ., 2, 55–65. https://doi.org/10.1007/s41748-018-0034-1

Ibrahim, M., Huo, A., Ullah, W., Ullah, S., & Xuantao, Z. (2025). An integrated approach to flood risk assessment using multi-criteria decision analysis and geographic information system. A case study from a flood-prone region of Pakistan. Front. Environ. Sci., 12, 1476761. https://doi.org/10.3389/fenvs.2024.1476761

Ibrahim, M., Huo, A., Ullah, W., Ullah, S., Ahmad, A., & Zhong, F. (2024). Flood vulnerability assessment in the flood prone area of Khyber Pakhtunkhwa, Pakistan. Front. Environ. Sci., 12, 1303976. https://doi.org/10.3389/fenvs.2024.1303976

Kelly, M., Schwarz, I., Ziegelaar, M., Watkins, A. B., & Kuleshov, Y. (2023). Flood risk assessment and mapping: a case study from Australia's Hawkesbury-Nepean catchment. Hydrology, 10, 26. https://doi.org/10.3390/hydrology10020026

Khan, I., Lei, H., Shah, A. A., Khan, I., & Muhammad, I. (2021). Climate change impact assessment, flood management, and mitigation strategies in Pakistan for sustainable future. Environ. Sci. Pollut. Res., 28, 29720–29731. https://doi.org/10.1007/s11356-021-12801-4

Khosravi, K., Pourghasemi, H. R., Chapi, K., & Bahri, M. (2016). Flash flood susceptibility analysis and its mapping using different bivariate models in Iran: a comparison between Shannon's entropy, statistical index, and weighting factor models. Environ. Monit. Assess., 188, 656–721. https://doi.org/10.1007/s10661-016-5665-9

Malczewski, J. (2000). On the use of weighted linear combination method in GIS: Common and best practice approaches. Transactions in GIS, 4(1), 5–22. https://doi.org/10.1111/1467-9671.00035

McFeeters, S. K. (1996). The use of the Normalized Difference Water Index (NDWI) in the delineation of open water features. International Journal of Remote Sensing, 17(7), 1425–1432. https://doi.org/10.1080/01431169608948714

Ming, X., Liang, Q., Dawson, R., Xia, X., & Hou, J. (2022). A quantitative multi-hazard risk assessment framework for compound flooding considering hazard inter-dependencies and interactions. J. Hydrology, 607, 127477. https://doi.org/10.1016/j.jhydrol.2022.127477

Mshelia, Z. H., Nyam, Y. S., Moisès, D. J., & Belle, J. A. (2024). Geospatial analysis of flood risk hazard in Zambezi Region, Namibia. Environ. Challenges, 15, 100915. https://doi.org/10.1016/j.envc.2024.100915

Nandi, A., Mandal, A., Wilson, M., & Smith, D. (2016). Flood hazard mapping in Jamaica using principal component analysis and logistic regression. Environ. Earth Sci., 75, 465–516. https://doi.org/10.1007/s12665-016-5323-0

Nasir, M. J., Iqbal, J., & Ahmad, W. (2020). Flash flood risk modeling of swat river sub-watershed: a comparative analysis of morphometric ranking approach and El-Shamy approach. Arabian J. Geosciences, 13, 1082–1119. https://doi.org/10.1007/s12517-020-06064-5

Olofsson, P., Foody, G. M., Herold, M., Stehman, S. V., Woodcock, C. E., & Wulder, M. A. (2014). Good practices for estimating area and assessing accuracy of land change. Remote Sensing of Environment, 148, 42–57. https://doi.org/10.1016/j.rse.2014.02.015

Paul, G. C., Saha, S., & Hembram, T. K. (2019). Application of the GIS-based probabilistic models for mapping the flood susceptibility in Bansloi sub-basin of Ganga-Bhagirathi river and their comparison. Remote Sens. Earth Syst. Sci., 2, 120–146. https://doi.org/10.1007/s41976-019-00018-6

Poussard, C., Dewals, B., Archambeau, P., & Teller, J. (2021). Environmental inequalities in flood exposure: a matter of scale. Front. Water, 3, 633046. https://doi.org/10.3389/frwa.2021.633046

Quesada-Román, A., & Campos-Durán, D. (2023). Natural disaster risk inequalities in Central America. Pap. Appl. Geogr., 9, 36–48. https://doi.org/10.1080/23754931.2022.2081814

Rahmati, O., Pourghasemi, H. R., & Zeinivand, H. (2016). Flood susceptibility mapping using frequency ratio and weights-of-evidence models in the Golastan Province, Iran. Geocarto Int., 31, 42–70. https://doi.org/10.1080/10106049.2015.1041559

Shafizadeh-Moghadam, H., Valavi, R., Shahabi, H., Chapi, K., & Shirzadi, A. (2018). Novel forecasting approaches using combination of machine learning and statistical models for flood susceptibility mapping. J. Environ. Manag., 217, 1–11. https://doi.org/10.1016/j.jenvman.2018.03.089

Shah, A. A., Ye, J., Abid, M., & Ullah, R. (2017). Determinants of flood risk mitigation strategies at household level: a case of Khyber Pakhtunkhwa (KP) province, Pakistan. Nat. Hazards J. Int. Soc. Prev. Mitig. Nat. Hazards, 88, 415–430. https://doi.org/10.1007/s11069-017-2872-9

Shah, S. M. H., Mustaffa, Z., Teo, F. Y., Imam, M. A. H., Yusof, K. W., & Al-Qadami, E. H. H. (2020). A review of the flood hazard and risk management in the South Asian Region, particularly Pakistan. Sci. Afr., 10, e00651. https://doi.org/10.1016/j.sciaf.2020.e00651

Sun, X., Jin, K., Tao, H., Duan, Z., & Gao, C. (2023). Flood risk assessment based on Hydrodynamic model—a case of the China–Pakistan economic corridor. Water, 15, 4295. https://doi.org/10.3390/w15244295

Tehrany, M. S., Lee, M.-J., Pradhan, B., Jebur, M. N., & Lee, S. (2014). Flood susceptibility mapping using integrated bivariate and multivariate statistical models. Environ. Earth Sci., 72, 4001–4015. https://doi.org/10.1007/s12665-014-3289-3

Tehrany, M. S., Pradhan, B., & Jebur, M. N. (2013). Spatial prediction of flood susceptible areas using rule based decision tree (DT) and a novel ensemble bivariate and multivariate statistical models in GIS. J. hydrology, 504, 69–79. https://doi.org/10.1016/j.jhydrol.2013.09.034

Toosi, A. S., Calbimonte, G. H., Nouri, H., & Alaghmand, S. (2019). River basin-scale flood hazard assessment using a modified multi-criteria decision analysis approach: a case study. J. Hydrology, 574, 660–671. https://doi.org/10.1016/j.jhydrol.2019.04.072

Tsakiris, G. (2007). Practical application of risk and hazard concepts in proactive planning. European Water, 19 (20), 47–56.

Tucker, C. J. (1979). Red and photographic infrared linear combinations for monitoring vegetation. Remote Sensing of Environment, 8(2), 127–150. https://doi.org/10.1016/0034-4257(79)90013-0

U.S. Geological Survey. (2021). Landsat Collection 2 (Fact Sheet 2021–3002). https://doi.org/10.3133/fs20213002

Ullah, F., Shah, S. A. A., Saqib, S. E., Yaseen, M., & Haider, M. S. (2021). Households' flood vulnerability and adaptation: Empirical evidence from mountainous regions of Pakistan. Int. J. Disaster Risk Reduct., 52, 101967. https://doi.org/10.1016/j.ijdrr.2020.101967

Ullah, K., & Zhang, J. (2020). GIS-based flood hazard mapping using relative frequency ratio method: a case study of Panjkora River Basin, eastern Hindu Kush, Pakistan. PLoS ONE15, e0229153. https://doi.org/10.1371/journal.pone.0229153

Ullah, K., Wang, Y., Fang, Z., Wang, L., & Rahman, M. (2022). Multi-hazard susceptibility mapping based on Convolutional neural networks. Geosci. Front., 13, 101425. https://doi.org/10.1016/j.gsf.2022.101425

Vojtek, M., & Vojteková, J. (2019). Flood susceptibility mapping on a national scale in Slovakia using the analytical hierarchy process. Water, 11, 364. https://doi.org/10.3390/w11020364

Wang, Z., Lai, C., Chen, X., Yang, B., Zhao, S., & Bai, X. (2015). Flood hazard risk assessment model based on random forest. J. Hydrology, 527, 1130–1141. https://doi.org/10.1016/j.jhydrol.2015.06.008

Waseem, M., Ahmad, S., Ahmad, I., Wahab, H., & Leta, M. K. (2023). Urban flood risk assessment using AHP and geospatial techniques in swat Pakistan. SN Appl. Sci., 5, 215 https://doi.org/10.1007/s42452-023-05445-1

Xu, H. (2006). Modification of normalised difference water index (NDWI) to enhance open water features in remotely sensed imagery. International Journal of Remote Sensing, 27(14), 3025–3033. https://doi.org/10.1080/01431160600589179

International Journal of Advanced Research